
This is an electronic reprint of the original article.
This reprint may differ from the original in pagination and typographic detail.

Beaumont, Marco; Rosenfeldt, Sabine; Tardy, Blaise L.; Gusenbauer, Claudia; Khakalo, Alexey; Nonappa; Opietnik, Martina; Potthast, Antje; Rojas, Orlando J.; Rosenau, Thomas
Soft cellulose II nanospheres

Published in:
Nanoscale

DOI:
[10.1039/c9nr05309c](https://doi.org/10.1039/c9nr05309c)

Published: 14/10/2019

Document Version
Peer-reviewed accepted author manuscript, also known as Final accepted manuscript or Post-print

Published under the following license:
Unspecified

Please cite the original version:
Beaumont, M., Rosenfeldt, S., Tardy, B. L., Gusenbauer, C., Khakalo, A., Nonappa, Opietnik, M., Potthast, A., Rojas, O. J., & Rosenau, T. (2019). Soft cellulose II nanospheres: Sol-gel behaviour, swelling and material synthesis. *Nanoscale*, 11(38), 17773-17781. <https://doi.org/10.1039/c9nr05309c>

This material is protected by copyright and other intellectual property rights, and duplication or sale of all or part of any of the repository collections is not permitted, except that material may be duplicated by you for your research use or educational purposes in electronic or print form. You must obtain permission for any other use. Electronic or print copies may not be offered, whether for sale or otherwise to anyone who is not an authorised user.

ARTICLE

Soft Cellulose II Nanospheres: Sol-Gel Behaviour, Swelling and Material Synthesis

Marco Beaumont,^{a,b*} Sabine Rosenfeldt,^c Blaise L. Tardy,^b Claudia Gusenbauer,^d Alexey Khakalo,^e Nonappa,^b Martina Opietnik,^f Antje Potthast,^a Orlando J. Rojas,^b Thomas Rosenau^{a,g*}

Received 00th January 20xx,
Accepted 00th January 20xx

DOI: 10.1039/x0xx00000x

High axial aspect crystalline nanomaterials have emerged as polymeric building blocks for the construction of supermaterials. In contrast to this form, amorphous nanospheres have remained largely untapped. This is especially peculiar in the context of material assembly, due to their wide range of opportunities by virtue of their soft particle characteristic, high volume ratio at low solid content and their highly swollen and accessible structure. In context of cellulose, these colloids represent a new field in the family of nanocelluloses. We report an organic solvent-free, heterogeneous and simple synthesis of spherical carboxylated nanoparticles bearing a distinctive, amorphous outer shell structure. The particle shape is evaluated by atomic force microscopy, cryo-transmission electron microscopy, dynamic light scattering and small-angle x-ray scattering. The soft shell structure of the particles and their responsiveness to ionic strength and pH are quantified by the combination of quartz-crystal microgravimetry and atomic force microscopy. Aqueous dispersions of the nanocolloids feature distinctive sol/gel behaviour: at solid content <2 wt% they behave as a low viscous liquid (sol state), whereas at higher concentrations the shells dominate the interparticle interactions, causing an exponential increase in viscosity, typical of a gel state (hydrogel). Gelation is reversible and can be triggered alternatively by protonation of the carboxylate groups in acidic condition. Supercritical drying of the hydrogels yields a highly porous, isotropic aerogel composed of aggregated nanoparticles. In contrast, ambient drying results in an anisotropic, fully transparent film. These colloids will allow the study of the interaction between soft cellulose and rigid matter, and have high potential as toughening additives in composites. Furthermore, the amorphous nature of the cellulosic nanoparticles of this new class of cellulose nanocolloids makes them attractive as support material for catalysts and enzymes.

Introduction

Cellulose is the most important structural polymer in nature, with crystal moduli in the range of 137 to 220 GPa^{1,2}, competitive to high-strength steel³ and carbon fibres⁴. Nanocelluloses belong to the most promising nanocolloids due to the ultra-strong mechanical properties, the high specific

surface area^{5,6} and the biocompatibility^{7,8}. The exploding number of publications in this field reflects their potential, especially in the form of cellulose nanofibrils (CNF) or nanocrystals (CNC). CNC are usually extracted by acidic hydrolysis⁹ of amorphous cellulose regions yielding rod-like, highly crystalline particles. Conducting this treatment in cold sulphuric acid enables control of crystallinity to obtain amorphous cellulose II nanoparticles^{13,14}. Spherical CNC counterparts, which are usually generated by acidic hydrolysis of regenerated cellulose (cellulose II crystal structure), are less common^{10–12}. Cellulose II nanospheres can be obtained from native cellulose I by homogeneous processes, through dissolution of cellulose and subsequent nanoprecipitation^{15–17}. In contrast, acid-free heterogeneous processes (thereby preserving the amorphous cellulose regions) to obtain cellulose II nanospheres start from cellulose II precursors^{18–20}. These precursors can be obtained at lab scales through caustic treatments of native cellulose^{19,20}. We reported a more promising and straightforward process to obtain spherical anionic NP (NPan)¹⁸, starting from a cellulose II precursor obtained in the lyocell process²¹ - an industrial process for man-made cellulosic fibres with a large production capacity. We showed that - in contrast to common cellulose II nanoparticle synthesis - involving acid-hydrolysis of amorphous regions^{10–12} of a cellulose II starting material, our procedure preserved the

^a Department of Chemistry, Institute of Chemistry for Renewable Resources, University of Natural Resources and Life Sciences Vienna (BOKU), Konrad-Lorenz-Straße 24, A-3430 Tulln, Austria.

^b Department of Bioproducts and Biosystems, School of Chemical Engineering, Aalto University, FI-00076 Aalto, Finland.

^c Bavarian Polymer Institute and Department of Chemistry, University of Bayreuth, D-95440 Bayreuth, Germany.

^d Department of Material Sciences and Process Engineering, Institute of Wood Technology and Renewable Materials, University of Natural Resources and Life Sciences (BOKU), Konrad-Lorenz-Straße 24, A-3430 Tulln, Austria.

^e VTT - Technical Research Centre of Finland, Tietotie 4E, P.O. Box 1000, FI-02044 Espoo, Finland.

KEYWORDS. Soft nanospheres, anisotropic nanogel, regenerated cellulose, lyocell process, cellulose II gel, carboxymethylated nanocellulose, mass-fractal superstructure.

*Corresponding author: thomas.rosenau@boku.ac.at; marcobeumont1@gmail.com

Electronic Supplementary Information (ESI) available: containing spectroscopic characterization by IR and NMR; determination of degree of substitution; crystallinity and zeta potential of starting material and product; influence of pH and mechanical treatment on particle size and colloidal stability; SAXS results and discussion, swelling behaviour in different ionic strengths; additional AFM, cryo-TEM images and rheological data. See DOI: 10.1039/x0xx00000x

amorphous, accessible regions²¹. The availability of this amorphous region makes the material attractive for subsequent adsorption or covalent introduction of chemical functionalities. Moreover, NPan is redispersible after drying by mild agitation. In contrast to nanocelluloses, generally available as dilute suspensions,²² NPan allows processing in dry state. Our preliminary results²¹ lead us to the at that time still unproven hypothesis that these particles were decorated with a soft and amorphous shell. These soft NPan would not only represent a new class of cellulose nanoparticles, but the proposed protocol was a very simple and efficient avenue towards spherical core-shell nanoparticles as well. In literature, this type of cellulose particles is mostly obtained starting from soluble cellulose-derivatives, including ethyl cellulose^{23,24}, cellulose xanthate²⁵ and others¹⁶. These synthesis routes are (i) homogeneous, (ii) require prior solubilisation of the cellulose by chemical or physical means, and (iii) are rather time-consuming and somewhat inefficient. In comparison to rigid/hard spheres, particles with a soft amorphous shell feature particular rheological properties²⁶: at low concentrations spherical core-shell NPs display a low apparent viscosity owing to their non-interacting behaviour; however, at a critical concentration the individual particles start to interact and partly overlap, causing a remarkable increase in viscosity, and eventually gelation. The amorphous characteristics and thereby high accessible particle volume of the shell makes these colloids especially attractive for applications as drug vehicle or catalyst support, especially if compared to cellulose nanocrystals^{27,28}. In addition, core-shell nanoparticles can be applied in composites to increase their toughness²⁹ a similar effect has recently been shown for the case of low-aspect ratio cellulose II nanoparticles³⁰. In this work, we used atomic force microscopy, cryo-transmission electron microscopy, dynamic light scattering, small-angle x-ray scattering and quartz-crystal microgravimetry (QCM), to unveil the core-shell structure of NPan. The effects of such structure on the rheological properties of NPan are studied, as well as the pH-dependent swelling behaviour of the amorphous particle shell. Depending on the drying method, the specific particle interactions cause the formation of either isotropic or anisotropic hierarchical structures. To the best of our knowledge this work represents the first structural study on a spherical, cellulose-based core-shell nanoparticle. In comparison to our previous organic solvent-based synthesis approach, we present here a simple and fully water-based route to "green" NPan. Given the availability of the precursor as an industrial product^{21,31} and the simple modification used, the new NPan approach represents a highly efficient way toward core-shell nanoparticles, which also could be easily scaled up, further increasing the significance of this work. Throughout our study, we used complementary characterisation techniques to evaluate the NPan structure and critically discuss their intrinsic core-shell and soft-matter features.

Experimental

The cellulose II gel also referred to as Lenzing™ lyocell gel^{21,31} (Lenzing™ is a registered trademark of Lenzing AG) with a solid

content of approx. 4 wt% was stored at 8°C until use. If not mentioned otherwise, all chemicals were acquired from Sigma-Aldrich. As a reference, cellulose nanofibrils were produced from fines-free (SCAN-M 6:69), fully bleached birch Kraft pulp (kappa number 1; DP 4700) by passing it seven times through a microfluidizer (Microfluidics M110P, Microfluidics Corporation, USA) at a pressure of 2000 bar to fibrillate the cellulose fibres into a stable colloidal dispersion of cellulose nanofibrils.

Synthesis of anionic nanoparticles (NPan)

The cellulose II gel was concentrated at 10000 rcf for 10 min to a solid content of 9.2 wt%. 32 g of this material (containing 2.9 g of dry cellulose, 18.2 mmol) was transferred into a 100 mL Schott bottle. The suspensions were stirred with a glass rod due to their high viscosity and a 50 wt% aqueous solution of NaOH (4.22 g, 52.8 mmol, 2.9 Eq) was added slowly to the stirred mixture. After 30 min, sodium chloroacetate (3.83 g, 32 mmol, 1.8 Eq) was added and the highly viscous gel was homogenised with a glass rod and transferred into a water bath shaker at 55°C. After 20 h, 60 mL of deionized water was added and the suspension was washed with distilled water followed by three washing and centrifugation cycles (5 min@10000 rcf). The suspension were further purified by dialysis (6-8 kDa regenerated cellulose membrane) against distilled water for 4 days. Finally, the suspensions were homogenised in a microfluidizer (Microfluidics M110P, Microfluidics Corporation, USA; 2 passes at 2000 bar) to yield spherical nanoparticles. The degree of substitution was determined by IR using the calibration curve in **Figure S1** (inset). Before size analysis, NPan was dispersed by ultra-sonication and centrifuged at 10000 rcf for 10 min, to remove NPan aggregates.

Particle size & electrostatic charge

The carboxymethylated cellulose II precursor was scanned by a laser diffraction particle size analyser (Mastersizer 2000, Malvern Instruments, UK), combining a blue and a red source at 470 and 632.8 nm wavelength, respectively.

The size of the nanoparticles was analysed using a Zetasizer Nanoseries (Malvern Instruments Ltd) at 25°C with 20 runs with a duration of 5 s. The measurement was repeated at least 6 times. Zeta potential and electrophoretic mobility measurements were performed on the same instrument at 25°C using a dip cell (Malvern Instruments Ltd). The nanoparticles were equilibrated in all cases in NaCl solution with different ionic strengths or buffers before measurement using 20 runs at 25°C (the measurement was repeated at least 5 times). The data was analysed by the Zetasizer software. The same buffers were used as in the case of QCM experiments, all buffers were adjusted to comparable ionic strength by addition of NaCl.

Cryogenic transmission electron microscopy (cryo-TEM)

Cryo-TEM imaging was performed on a Jeol 3200FSC (JEOL, USA) operating at 300 kV in bright field mode. The images were acquired with an Omega-type Zero-loss energy filter and captured with a Gatan Ultrascan 4000 CCD camera. The microscope was cooled down with liquid nitrogen and the

sample temperature was maintained at $-187\text{ }^{\circ}\text{C}$ throughout the imaging. $3\text{ }\mu\text{L}$ of the sample dispersion at a concentration of $0.1\text{ wt}\%$ was transferred on a Quantifoil R 2/1 Holey carbon (Cu 200 Mesh) grid in $100\text{ }\%$ humidity. Excess amount of sample was blotted away with filter paper for 3 s and the samples were plunged into $-170\text{ }^{\circ}\text{C}$ ethane/propane ($1/1\text{ v/v}$) mixture using FEI Vitrobot Mk3. The vitrified samples were cryo-transferred to the microscope for imaging. The micrographs were analysed with the software ImageJ³².

Quartz crystal microgravimetry (QCM)

Interactions between surface-immobilised NPan and CNF were investigated on gold-coated sensors and a quartz crystal microbalance with dissipation unit (QCM-D, E4 instrument, Q-Sense AB, Sweden). The sensors were first cleaned with UV/ozone treatment for 15 min followed by polyethyleneimine adsorption from a $0.1\text{ wt}\%$ aqueous solution for 15 min . After thorough rinsing with Milli-Q water, all crystals were dried with nitrogen gas. All solutions were filtered using $0.45\text{ }\mu\text{m}$ filters. The NPan and CNF dispersions were pre-treated by ultrasonication (10 min at an amplitude of 25%) and centrifuged for 45 min at 10000 rcf . For swelling experiments with NPan and CNF, the materials were adsorbed on a polyethyleneimine-coated gold crystal during the QCM measurement. Swelling studies at $\text{pH } 3$, $\text{pH } 7$ and $\text{pH } 11$ were conducted using 10 mM citric acid, phosphate and carbonate buffers (with a similar ionic strength of 20 mM), respectively. The QCM experiments were performed at a constant flow rate of $100\text{ }\mu\text{L}/\text{min}$ and the temperature was maintained at $23\text{ }^{\circ}\text{C}$.

Atomic Force Microscopy (AFM)

The surface topography of the particles was studied on polyethyleneimine-coated SiO_2 wafers and native SiO_2 wafers by a Nanoscope IIIa multimode scanning probe microscope (Digital Instruments, USA). Surface areas of 3×3 and $1 \times 1\text{ }\mu\text{m}^2$ were investigated in air using tapping mode with silicon cantilevers. Images were processed (flattening) and analysed with Gwyddion software.

Imaging of wet samples was performed on the as-obtained QCM sensors, coated with a dense layer of nanoparticles. The solution evaluated consisted of dilute solutions of citric acid, phosphate and carbonate buffer as used in the QCM experiments. The cantilever had a nominal resonance frequency of ca. 300 kHz , a tip radius of curvature of 8 nm and a half cone angle of 20° . Imaging was performed in tapping mode after equilibration for approx. 1 h . Analysis was performed using ImageJ software.

Solid-state nuclear magnetic resonance (NMR) experiments

Solid-state NMR experiments were done on a Bruker Avance III HD 400 spectrometer with a 4 mm dual broadband CP-MAS probe, as described previously²¹. Peak fitting was performed with the Dmfit program. All materials for solid-state NMR were freeze-dried before measurement³³.

Small Angle X-ray Scattering (SAXS)

The samples were measured as received under standard conditions, e.g. as dispersion in 1 mm glass capillaries (Hilgenberg, Germany, inner diameter 0.98 mm) or as free standing film parallel to the incident X-ray beam. All small angle X-ray scattering (SAXS) data reported here were performed on the small-angle X-ray system "Double Ganesha AIR" (SAXSLAB, Denmark). The X-ray source of this laboratory-based system is a rotating anode (copper, MicoMax 007HF, Rigaku Corporation, Japan). The data were recorded by a position sensitive detector (PILATUS 300K, Dectris). To cover the range of scattering vectors q , different detector positions were used ($q = |\vec{q}| = \frac{4\pi}{\lambda} \sin(\frac{\theta}{2})$), where λ is the wavelength and θ is the scattering angle. The circularly averaged data were normalised to incident beam, and assumed a sample thickness of 1 mm and measurement time before subtraction of the (solvent) background. SAXS fits in **Figure S3** were performed using SasFit 0.94.1 software.³⁴

Results and discussion

NPan were synthesised by carboxymethylation of particular cellulose II specimens (**Figure 1**, left) at a high cellulose solid content ($\sim 9\text{ wt}\%$) yielding a carboxymethylated sample with a degree of substitution of 0.1 . Infrared (IR) and solid-state nuclear magnetic resonance (NMR) spectra of NPan are shown in **Figure S1** and clearly demonstrate the successful functionalisation. Conducting the synthesis at high solid content allowed us to avoid organic solvents and time-consuming solvent-exchange steps that previously were still necessary¹⁸; the here-reported method is aqueous and organic solvent-free throughout. **Table S1** shows that the crystalline structure was only slightly affected by carboxymethylation. At a NPan crystallinity of 49% there is a considerably high amount of non-ordered, amorphous cellulose present, which is in contrast to the results from acidic protocols to extract cellulose nanocrystals from biomass^{11,35}. The fact that the crystallinity of NPan is in the same order as the crystallinity degree of the raw material (the cellulose II precursor having 47% crystallinity), shows that the modification is confined to the amorphous and thus better accessible regions of the material, the crystalline and inaccessible ones not being functionalized by this treatment. Mechanical treatment of this functional precursor, which is decorated with negative and repulsive carboxylate groups, yields spherical nanoparticles as was reported in our previous publication.¹⁸

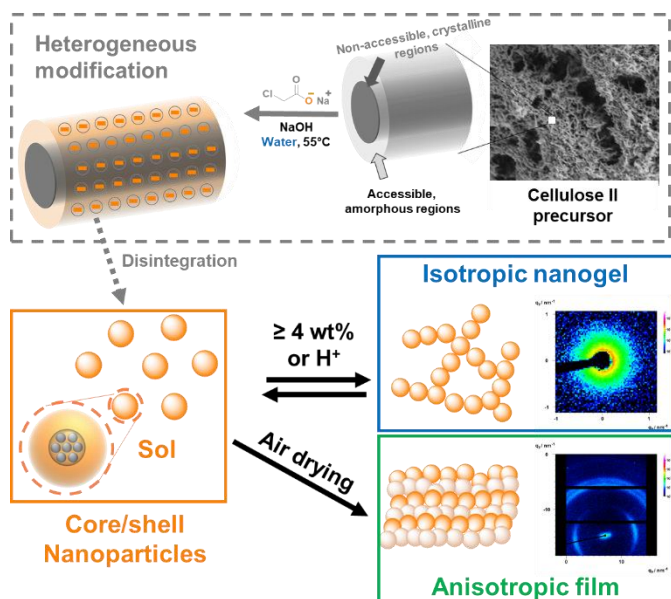


Figure 1: Synthesis of anionic nanoparticles (NPan) from a cellulose II precursor. Heterogeneous modification by carboxymethylation results in selective modification of the accessible cellulose regions. Subsequent disintegration gives results in the formation of nanoparticles with a more crystalline core and an amorphous, highly carboxymethylated shell. The NPan features sol-gel behaviour: at low concentration NPan is sol-like and, low- viscous, whereas at concentration exceeding 4 wt%, a gel-like behaviour dominates, yielding a hydrogel. Air drying of NPan causes particle alignment into a film. 2D-Small angle X-ray scattering measurements show the isotropic structure of the gel (top right inset) and the anisotropic alignment in the film (bottom right inset).

The effect of the treatment severity on the particle size is illustrated in **Figure S2A**. Individualised nanoparticles were obtained already after two passes in a microfluidizer. Next, we thoroughly evaluated the physico-chemical characteristics of the NPan, in particular the structure/property relationship of the intrinsic core-shell structure with respect to rheology, swelling, adsorption behaviour and surface/particle and inter-particle interactions. The particles were shown to be in the nanoscale and spherical in shape (cryo-TEM, AFM and DLS in **Figure 2**).

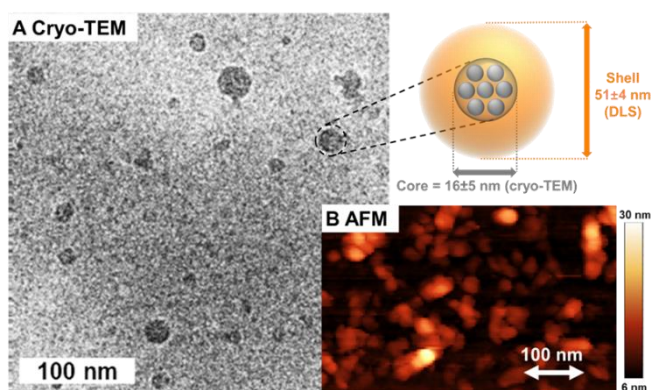


Figure 2: Shape, size and structure of the anionic cellulose II nanoparticles studied by cryo-transmission electron microscopy (TEM) (A) and (AFM) (B). The particles consist of a core-shell structure. The semi-crystalline core was visualised by cryo-TEM, whereas the size of the accessible and hydrated outer shell was determined by DLS.

As illustrated in **Figure 1 (right)**, at a solid contents > 4 wt%, the nanoparticles formed a hydrogel. Small-angle-X-ray scattering (SAXS) measurements on NPan sol (1 wt%) and NPan gel (4 wt%) (**Figure 1 top right, Figure S4A**) both feature isotropic behaviour, whereas the dried film (**Figure 1 bottom right, Figure S4B**) clearly reveals anisotropy due to structural alignment into a sheet-like sub-structure.

Details about the size and structure of the particles were unveiled by cryo-TEM, which was applied to avoid any drying effect artefacts, which might obscure the analysis. Cryo-TEM micrographs (**Figure 2A, zoom of Figure S4C**) yielded an average particle size of 16 ± 5 nm. AFM height profiles of NPan gave a comparable value, 22 ± 7 nm (**Figure 2B, magnification from Figure S4A**). These values correspond well to the diameter of non-anionic spherical cellulose II nanoparticles from the literature^{11,19}. However, the hydrodynamic diameter of the particles measured by DLS was much higher with an averaged hydrodynamic diameter of 51 ± 4 nm and a polydispersity index of 0.21 ± 0.04 . This was a first indication of the highly amorphous NPan shell structure due to its associated swelling behaviour, schematically shown in **Figure 2**. The solvent-swollen nature of the shell causes a very low TEM and SAXS contrast (the excess electron density distribution in both cases), so that cryo-TEM and SAXS measurements take into account mainly the contributions of the crystalline particles region. From these results we derived a core diameter of approx. 16 nm equalling $d(\text{cryo-TEM})$ and a shell thickness of 18 nm (difference of $d(\text{DLS})$ and $d(\text{cryo-TEM})$). SAXS analysis gave further insights into the core structure and revealed that it features a fractal structure composed of individual crystallites (see **Figure S3** and supporting information for details).

Studying the effect of size on particle concentration, we observed a deswelling phenomenon at increasing particle concentration (**Figure S2C**): the number-average particle size was clearly reduced from approx. 67 nm at 0.05 wt% to 28 nm at 0.5 wt%. Based on literature³⁶, we conclude that at low particle concentration the shell is highly extended to minimize electrostatic repulsive forces between the carboxylate groups. At higher concentration, however, the effect of repulsive forces of neighbouring particles dominates and the particle shells contract (the increase of concentration causes as well some minor particle aggregation, as seen from an increase of the z-average particle size). In addition, we examined the effect of ionic strength on the particle size (particle shell extension). As shown in **Figure S2D**, an increase of ionic strength first causes a reduction in particle size (z-average and number-average size): the particle shell shrinks due the shielding effect of the ions reducing repulsive forces between carboxylate groups. Ionic strengths above 25 mM decrease colloidal stability of the particle dispersion causing aggregation and an increase in the particle size. A study of NPan in different phosphate buffers (5 mM and 10 mM) produced similar effects on the particle structure (**Figure S2E**). These results further corroborate the core-shell particle structure consisting of a soft and amorphous shell and semi-crystalline core.

To further elucidate the soft-matter characteristics of the particles, we studied their swelling behaviour in different buffer

solutions by a quartz crystal microbalance (QCM). The QCM crystals were coated beforehand with a polyethyleneimine monolayer. The effect of this layer on the QCM experiment can be neglected due to its low thickness of 0.6 nm³⁷. NPan and CNF were adsorbed during the QCM experiment onto the polyethyleneimine-coated QCM crystals through electrostatic interactions (Figure S5). After the QCM experiment, the same crystals were analysed with AFM to show that the introduced cellulose particles were not desorbed upon buffer changes. The adsorption of CNF decreased the QCM frequency to a larger extent (approx. -70 Hz) in comparison to the adsorption of NPan (approx. -22 Hz).

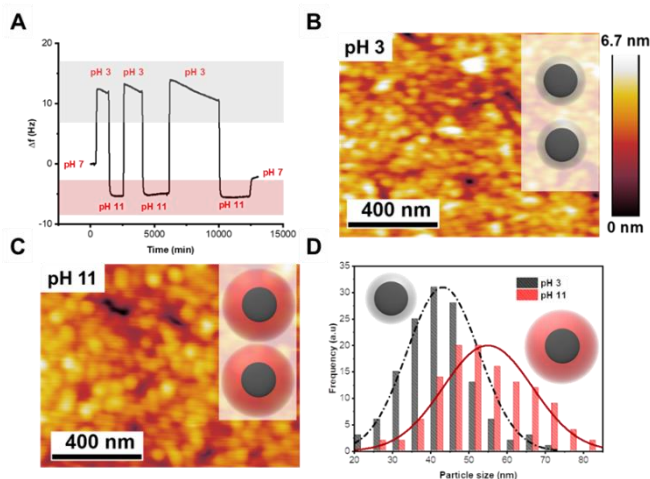


Figure 3: Swelling behaviour of the spherical, anionic cellulose II nanoparticles (NPan) in acidic and alkaline buffer solutions measured on a quartz crystal microbalance (A, grey shading represents a contracted NPan state and red shading a swollen one), liquid AFM scanning of NPan (B-C) and particle size distribution from AFM analysis (D). The amorphous shell of the particles swells and expands under alkaline conditions (deprotonation of carboxylic acids to carboxylate) and collapses in acidic media (reprotonation of carboxylate to carboxylic acid moieties).

This indicates that a larger effective mass of CNF was adsorbed. In contrast, the effect of changes in buffer solution were more dramatic in the case of NPan. This can be explained by the soft and amorphous shell of NPan, which is highly sensitive to ionic strength and buffer composition (see QCM profiles after exchange of water with 10 mM NaCl and buffer of pH 7, Figure S5). We further studied the pH-dependent swelling behaviour of NPan by QCM (Figure 3A) and AFM (Figure 3B-D).

In acidic medium, the carboxylate exists in its protonated form and the particles shell collapses, as seen in the increase in QCM frequency, indicating a weight loss due to removal of water. On the contrary, at alkaline pH, the frequency shift in the QCM experiment is reduced, indicating that the particle shell swells (absorbs water) (Figure 3A). This process is reversible, as shown in the QCM profiles. To further prove the swelling capability of the particles, AFM analyses in liquid media were performed using the same sample (NPan on QCM sensor) and the same buffer solutions. In this case, the samples were dried after the QCM experiments and rewetted in the respective buffer solution. The swelling effects can be clearly observed with the AFM analyses. At pH 3 (Figure 3B), the particle is in contracted state due to the protonation and collapse of the NPan shell. In contrast, at pH 11 (Figure 3C), the NPan is in swollen state

(carboxyl groups are deprotonated) is therefore higher than in the previous acidic pH (Figure 3D). This shows that even after drying and rewetting, the cellulose particles swell considerably. The swelling of NPan was further confirmed quantitatively by liquid AFM scanning, which showed a change in hydrodynamic particle diameter at different pH values (Figure 3D). At pH 3 the average particle size was 43 ± 8 nm and under basic conditions (pH 11) 54 ± 13 nm. In this context we want to mention that usually cellulose swelling after water removal³⁸ and especially after severe thermal drying is strongly reduced by partly irreversible “crosslinking”, often called hornification, due to irreversible bond formation between neighbouring cellulose chains and surface sealing.

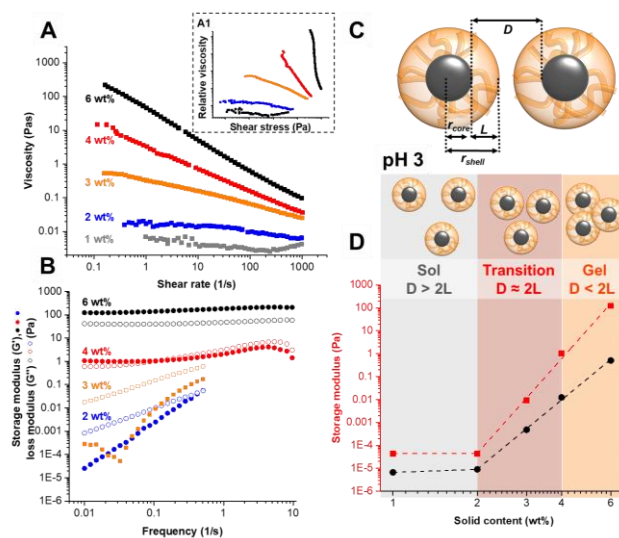


Figure 4: Rheology of NPan: Viscosity curves (A), dependence of the shear stress on the relative viscosity (inset A1) and shear moduli of NPan (B) at different solid contents. Schematic representation of the mean core surface-to-surface distance D of two nanoparticles (C). At low solid content (≤ 2 wt%), the core-shell particles are individually dispersed, and the effect of the solid content on the storage modulus and viscosity (D) is very low. Higher concentration causes an increase in storage modulus and viscosity, especially in the gel regime (≥ 4 wt%), due to strong interactions between neighbouring nanoparticles. Note that all graphs are in logarithmic scale.

Regarding the QCM results, the difference between the swollen and collapsed NPan is smaller than expected from the cryo-TEM and DLS studies in Figure 2. To explain this, one must take into account that the particles on the crystal sensor do not form a single layer, but rather a fused film. The swelling of individual particles is finally influenced by neighbouring particles in the film. NPan features a moderate zeta potential of -30 mV in 2.5 mM aqueous NaCl solution (see Table S1), indicating a colloidally stable dispersion of NPan³⁹. However, it is important to keep in mind that the mobility of soft particles is insensitive to the precise position of the slipping plane so that the zeta potential loses its physical meaning⁴⁰. We therefore used the electrophoretic mobility to study the effects of ionic strength and pH on the colloids.

The electrophoretic mobility of NPan at different pH values (Figure S2B), shows the mobility to be very similar under neutral or alkaline conditions (due to similar ionic strengths of the buffers). At acidic conditions, the negative electrophoretic

mobility increases as well as the particle size: protonation of carboxylate groups decreases particle charge and increases particle size due to aggregation. The dependence of the ionic strength on electrophoretic mobility of NPan (**Figure S2F**) is reflected in an increase of the negative mobility at increasing ionic strength, attributable to ion shielding and reduction of the particle charge⁴⁰. In addition, we noticed that the effect of ionic strength is less pronounced in case of NPan if compared to hard cellulose nanocrystals (**Figure S2F**), which is in accordance to the theories of electrophoresis of soft colloids⁴⁰.

At low solid contents (< 3 wt%), NPan dispersions display a low apparent viscosity and a dominating viscous behaviour ($G'' > G'$) at low frequencies, see **Figure 4A** and **4D**⁴¹. In comparison, the viscosity of a CNC dispersion at 1 wt% is approx. 0.2 Pas⁴², 20 times higher than the viscosity of NPan at the same solids content. This can be reasoned by the lower aspect ratio of NPan in comparison to CNC (spherical vs. rod-like shapes). Hence, interparticle interactions are smaller in the case of NPan. This is also reflected in **Figure 4A1**: the relative viscosity of the diluted particle dispersion (1 and 2 wt%) is only slightly affected by the shear stress. At 3 wt%, the viscosity increases significantly, a low-shear Newtonian plateau is observed followed by a shear-thinning region at higher shear stress. At higher solid contents the low-shear Newtonian plateau disappears, and yield stress develops. This phenomenon corresponds to the overlap of the particle shells at volume fractions higher than the critical volume fraction of the particles core, ϕ^* .²⁶ In **Figure 4C**, the mean surface-to-surface distance (D) between two individual cores is schematically shown.

Here, D is related to the volume fraction of the particle cores, ϕ and the core radius, r_{core} ²⁶:

$$D = 2r_{core} \left(\frac{0.637}{\phi} \right)^{1/3} - 2r_{core} \quad (\text{Eq. 1})$$

At ϕ^* , $D = 2L$ (L is the difference between the shell radius, r_{shell} , and the core radius, r_{core}).

$$\phi^* = 0.637 \left(\frac{r_{core}}{r_{shell}} \right)^3 \quad (\text{Eq. 2})$$

ϕ^* can be calculated using Eq. 2. We used r_{core} from cryo-TEM and r_{shell} from DLS data (**Figure 2**) and obtained a critical core volume fraction of 2 vol% (note that due to the extended nature of the shell the actual NPan volume fraction is much higher). In order to determine the critical solid content, we took into account the crystallinity of NPan and approximated that the mass of the particle cores corresponds to 70% of the total mass. The calculated critical solid content, i.e., critical particle concentration, was 4 wt%, which agrees well with the rheology measurements. At the theoretical critical particle concentration (4 wt%), the viscosity of NPan was 150 times higher than at 2 wt%. With respect to the shear moduli in **Figure 4B**, this solid content represents not only the calculated critical particle concentration, but also the gel point of NPan. This is also shown in the frequency-dependency profile of the loss tangent in **Figure S6**. At higher solid contents, NPan can be classified as rheological gel ($G' > G''$ at low frequencies) and the viscosity increases with concentration, as shown in **Figure 4A** and **4D**. The

deviation of the properties (viscosity and shear moduli) from the initial rheology (solid content ≤ 2 wt%) is a result of shell-shell interactions and overlapping of individual NPan nanoparticles, causing an exponential increase in viscosity and storage modulus. The presence of the particle shells also explains the lower gel point of NPan (4 wt%) in comparison to that of rigid CNC (at 10 wt%)⁴². The gelation of NPan is reversible upon dilution and can be triggered as well by acidic treatment through protonation of the carboxylate groups (**Figure S7A**). The gelation tendency at low pH is also reflected in the zeta-potential and particle size measurements (**Figure S2B**).

With regard to the role of particle interactions upon drying and their effect in the formation of 2D and 3D materials, we found that structuring of NPan upon drying can be controlled by varying the drying process to obtain either isotropic aerogels (3D) or anisotropic films (2D) (**Figure 5**). The 2D-SAXS data of both structure aggregates are shown in **Figure 1**. NPan above the gel point, did not flow upon vial inversion (**Figure 5A**). As schematically shown in **Figure 4C** and further discussed in the rheology section, we attribute this gelation to overlapping of individual NPan particles into a super-structured fractal network. In principle, water removal of diluted NPan by ambient drying is expected to yield a gelled NPan. Further water removal and structure densification caused an anisotropic alignment of the NPan in a film as shown in **Figure 5B**.

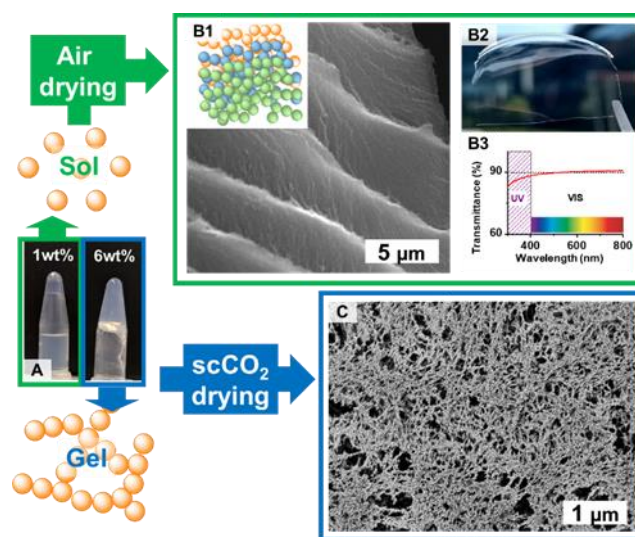


Figure 5: Nanoparticle dispersions in sol and gel state (A). Air drying of NPan sol causes alignment into an anisotropic sheet structure (SEM in B1, top view of fracture) in form of a highly transparent film (B2 and B3). In contrast to this, supercritical drying of a gelled sample yields a porous, isotropic aerogel structure (C).

AFM topography confirms that the film comprises individual nanoparticles (**Figure S7B**). This anisotropic film is expected to feature promising optical properties. Notably, the films are highly transparent (**Figure 5B2 and B3**). The 1D-SAXS pattern of the film in **Figure S3A** fits very well to the lamellar sheet-like structure, which is shown in **Figure 5B1**, and further supports that the film consists of subunits with a correlation distance of approx. 4 nm. This size corresponds to the crystallite size of the cellulose II structure (**Table S1**), the core of NPan thus

resembling a fractal object consisting of 4 nm crystallites. SAXS analysis of the NPan dispersions in **Figure S3B** further confirmed this structure. This is discussed in more detail in the supporting information.

Supercritical drying of this NPan gel produced a highly porous isotropic aerogel comprising a fibrillar superstructure (**Figure 5C**), which is similar to the structure of the cellulose II precursor of NPan⁴³. Note that the average diameter, obtained from the SEM micrograph was 27±8 nm (including 5 nm gold coating), comparable to the particle size from AFM and cryo-TEM (**Figure 2**). Thus, gelling of NPan is caused by overlapping and densification of individual particle shells into a fibrillar, isotropic network.

Conclusions

Anionic cellulose nanoparticles (NPan) derived from regenerated cellulose (cellulose II) were prepared by straightforward organic solvent-free, heterogeneous synthesis. NPan feature an intrinsic solid core / soft shell structure, as confirmed by studies on swelling and sol-gel behaviour combined with structural analysis using AFM, cryo-TEM and DLS. NPan have an average core diameter of approx. 16 nm with and a shell thickness of 18 nm. SAXS scattering patterns gave further insight into the structure and revealed that the particle core is semi-crystalline consisting of 4 nm-sized crystallites. Microgravimetric studies showed distinctive swelling of the shell under basic condition and collapsing under at acidic conditions, as also confirmed by AFM analysis in liquid medium. NPan have low viscosity under dilute conditions. At higher solid contents (> 3 wt%), individual particle shells start to interact/overlap with each other forming a network structure. Viscosity and shear moduli increase exponentially until a highly viscous gel is formed at 4 wt%. Supercritical drying of the isotropic NPan in gel state, yields a dense aerogel structure. Further structure densification caused formation of an anisotropically ordered, highly transparent (90% transparency) film with a multilamellar substructure. The reported cellulose II nanoparticles can be efficiently produced and feature unique properties due to their intrinsic core-shell structure. This new class of cellulose colloids will enable the study of interactions and synergies between soft nanocelluloses and rigid matter. Due to the highly accessible outer region, NPan might allow the synthesis of carrier material for active compounds, such as catalysts or enzymes.

Conflicts of interest

There are no conflicts to declare.

Acknowledgements

We would like to acknowledge the financial support in the framework of Austrian Biorefinery Center Tulln. The authors also thank H2020-ERC-2017-Advanced Grant "BioELCell"

(788489) and COST Action FP1205 for funding support. We are grateful to Lenzing AG for supplying cellulose II gel samples.

References

- 1 I. Sakurada, Y. Nukushina and T. Ito, *J. Polym. Sci.*, 1962, **57**, 651–660.
- 2 I. Diddens, B. Murphy, M. Krisch and M. Müller, *Macromolecules*, 2008, **41**, 9755–9759.
- 3 Wang Wei-yong, Liu Bing and Kodur Venkatesh, *Journal of Materials in Civil Engineering*, 2013, **25**, 174–182.
- 4 National Research Council, *High-Performance Structural Fibers for Advanced Polymer Matrix Composites*, The National Academies Press, Washington, DC, 2005.
- 5 L. Heath and W. Thielemans, *Green Chemistry*, 2010, **12**, 1448.
- 6 S. F. Plappert, J.-M. Nedelec, H. Rennhofer, H. C. Lichtenegger and F. W. Liebner, *Chemistry of Materials*, 2017, **29**, 6630–6641.
- 7 M. Bhattacharya, M. M. Malinen, P. Lauren, Y.-R. Lou, S. W. Kuisma, L. Kanninen, M. Lille, A. Corlu, C. GuGuen-Guillouzo, O. Ikkala, A. Laukkanen, A. Urtti and M. Yliperttula, *Journal of Controlled Release*, 2012, **164**, 291–298.
- 8 A. Sinha, E. M. Martin, K.-T. Lim, D. J. Carrier, H. Han, V. P. Zharov and J.-W. Kim, *Journal of Biosystems Engineering*, 2015, **40**, 373–393.
- 9 Y. Habibi, L. A. Lucia and O. J. Rojas, *Chem. Rev.*, 2010, **110**, 3479–3500.
- 10 M. Cheng, Z. Qin, Y. Liu, Y. Qin, T. Li, L. Chen and M. Zhu, *J. Mater. Chem. A*, 2014, **2**, 251–258.
- 11 C.-F. Yan, H.-Y. Yu and J.-M. Yao, *Cellulose*, 2015, 3773–3788.
- 12 J. Zhang, T. J. Elder, Y. Pu and A. J. Ragauskas, *Carbohydrate Polymers*, 2007, **69**, 607–611.
- 13 M. Loelovich, *Nanoscience and Nanotechnology*, 2012, **2**, 9–13.
- 14 M. Loelovich, *ISRN Chemical Engineering*, 2012, **2012**, 1–7.
- 15 T. Liebert, M. Kostag, J. Wotschadlo and T. Heinze, *Macromol. Biosci.*, 2011, **11**, 1387–1392.
- 16 M. Nikolajski, J. Wotschadlo, J. H. Clement and T. Heinze, *Macromolecular Bioscience*, 2012, **12**, 920–925.

- 17C. Carrick, L. Wågberg and P. A. Larsson, *ACS Macro Lett.*, 2014, **3**, 1117–1120.
- 18M. Beaumont, T. Nypelö, J. König, R. Zirbs, M. Opietnik, A. Potthast and T. Rosenau, *Green Chem.*, 2016, **18**, 1465–1468.
- 19L.-Q. Zhang, B. Niu, S.-G. Yang, H.-D. Huang, G.-J. Zhong and Z.-M. Li, *ACS Sustainable Chemistry & Engineering*, 2016, **4**, 2470–2478.
- 20H.-Q. Wang, H. Tan, S. Hua, Z.-Y. Liu, W. Yang and M.-B. Yang, *Macromolecular Rapid Communications*, 2017, **38**, 1700409.
- 21M. Beaumont, H. Rennhofer, M. Opietnik, H. C. Lichtenegger, A. Potthast and T. Rosenau, *ACS Sustainable Chemistry & Engineering*, 2016, **4**, 4424–4432.
- 22M. Beaumont, A. Potthast and T. Rosenau, in *Cellulose Science and Technology*, eds. T. Rosenau, A. Potthast and J. Hell, John Wiley & Sons, Inc., Hoboken, NJ, USA, 2018, pp. 277–339.
- 23W. Liu, R. Liu, Y. Li, H. Kang, D. Shen, M. Wu and Y. Huang, *Polymer*, 2009, **50**, 211–217.
- 24Y.-L. Yu, M.-J. Zhang, R. Xie, X.-J. Ju, J.-Y. Wang, S.-W. Pi and L.-Y. Chu, *Journal of Colloid and Interface Science*, 2012, **376**, 97–106.
- 25S. Nagaoka, T. Jodai, Y. Kameyama, M. Horikawa, T. Shirosaki, N. Ryu, M. Takafuji, H. Sakurai and H. Ihara, *RSC Advances*, 2016, **6**, 33036–33042.
- 26C. L. A. Berli and D. Quemada, *Langmuir*, 2000, **16**, 7968–7974.
- 27C. Chen, R. A. L. Wylie, D. Klinger and L. A. Connal, *Chem. Mater.*, 2017, **29**, 1918–1945.
- 28R. Beltrán-Suito, P. W. Menezes and M. Driess, *Journal of Materials Chemistry A*, , DOI:10.1039/C9TA04583J.
- 29H. He, T. E. Tay, Z. Wang and Z. Duan, *J Mater Sci*, 2019, **54**, 4984–4996.
- 30J. Antti Sirviö, *Journal of Materials Chemistry A*, 2019, **7**, 755–763.
- 31WO/2015/054712, 2015.
- 32C. A. Schneider, W. S. Rasband and K. W. Eliceiri, *Nat Meth*, 2012, **9**, 671–675.
- 33D. Massiot, F. Fayon, M. Capron, I. King, S. Le Calvé, B. Alonso, J.-O. Durand, B. Bujoli, Z. Gan and G. Hoatson, *Magn. Reson. Chem.*, 2002, **40**, 70–76.
- 34I. Breßler, J. Kohlbrecher and A. F. Thünemann, *J Appl Cryst*, 2015, **48**, 1587–1598.
- 35G. Sèbe, F. Ham-Pichavant, E. Ibarboure, A. L. C. Koffi and P. Tingaut, *Biomacromolecules*, 2012, **13**, 570–578.
- 36S. Nöjd, P. Holmqvist, N. Boon, M. Obiols-Rabasa, P. S. Mohanty, R. Schweins and P. Schurtenberger, *Soft Matter*, 2018, **14**, 4150–4159.
- 37H.-J. Yun, H. Hong, J. Lee and C.-J. Choi, *Mater. Trans.*, 2014, **55**, 801–805.
- 38J. M. B. Fernandes Diniz, M. H. Gil and J. A. A. M. Castro, *Wood Science and Technology*, 2004, **37**, 489–494.
- 39A. S. Dukhin and P. J. Goetz, *Studies in interface science*, 2002, **15**, 1–372.
- 40H. Ohshima, *Colloids and Surfaces A: Physicochemical and Engineering Aspects*, 1995, **103**, 249–255.
- 41K. Almdal, J. Dyre, S. Hvidt and O. Kramer, *Polymer Gels and Networks*, 1993, **1**, 5–17.
- 42C. Qiao, G. Chen, J. Zhang and J. Yao, *Food Hydrocolloids*, 2016, **55**, 19–25.
- 43M. Beaumont, A. Kondor, S. Plappert, C. Mitterer, M. Opietnik, A. Potthast and T. Rosenau, *Cellulose*, 2017, **24**, 435–440.